ACS OMEGA

http://pubs.acs.org/journal/acsodf

Article

$Fe_4(OAc)_{10}[EMIM]_2$: Novel Iron-Based Acetate EMIM Ionic Compound

Godwin Severa,* Edward Bruffey, Phuong Q. H. Nguyen, Angelina Gigante, Noemi Leick, Colleen Kelly, Gregory J. Finkelstein, Hans Hagemann, Thomas Gennett, Richard E. Rocheleau, and Przemyslaw Dera*

Cite This: *ACS Omega* 2021, 6, 31907−31918

Read Online

ACCESS | Metrics & More | Article Recommendations | Supporting Information

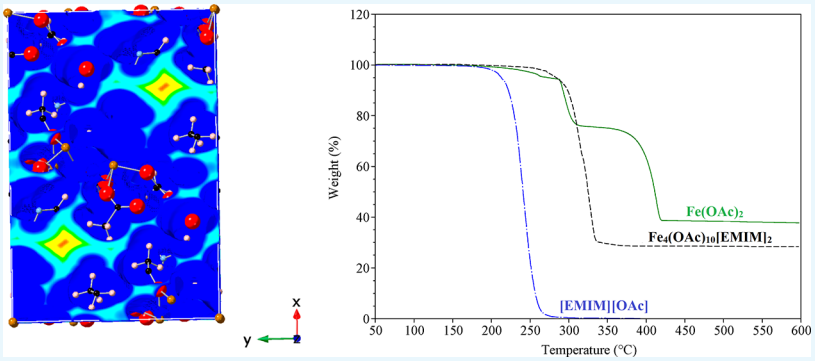

ABSTRACT: We synthesized and characterized a novel iron(II) aceto EMIM coordination compound, which has a simplified empirical formula $Fe_4(OAc)_{10}[EMIM]_2$, in two different hydration forms: as anhydrous monoclinic compound and triclinic dihydrate $Fe_4(OAc)_{10}[EMIM]_2{\cdot}2H_2O$. The dihydrate compound is isostructural with recently reported $Mn_4(OAc)_{10}[EMIM]_2{\cdot}2H_2O$, while the anhydrate is a superstructure of the Mn counterpart, suggesting the existence of solid solutions. Both new Fe compounds contain chains of Fe^{2+} octahedrally coordinated exclusively by acetate groups. The EMIM moieties do not interact directly with the Fe^{2+} and contribute to the structural framework of the compound through van der Waals forces and C−H···O hydrogen bonds with the acetate anions. The compounds have a melting temperature of ∼94 °C; therefore, they can be considered metal-containing ionic liquids. Differential thermal analysis indicates three endothermic transitions associated with melting, structural rearrangement in the molten state at about 157 °C, and finally, thermal decomposition of the $Fe_4(OAc)_{10}[EMIM]_2$. Thermogravimetric analyses indicate an ∼72 wt % mass loss during the decomposition at 280−325 °C. The $Fe_4(OAc)_{10}[EMIM]_2$ compounds have higher thermal stability than their Mn counterparts and [EMIM][OAc] but lower compared to iron(II) acetate. Temperature-programmed desorption coupled with mass spectrometry shows that the decomposition pathway of the $Fe_4(OAc)_{10}[EMIM]_2$ involves four distinct regimes with peak temperatures at 88, 200, 267, and 345 °C. The main species observed in the decomposition of the compound are CH_3, H_2O, N_2, CO, $OC{-}CH_3$, $OH{-}CO$, $H_3C{-}CO{-}CH_3$, and $H_3C{-}O{-}CO{-}CH_3$. Variable-temperature infrared vibrational spectroscopy indicates that the phase transition at 160−180 °C is associated with a reorientation of the acetate ions, which may lead to a lower interaction with the $[EMIM]^+$ before the decomposition of the $Fe_4(OAc)_{10}[EMIM]_2$ upon further heating. The $Fe_4(OAc)_{10}[EMIM]_2$ compounds are porous, plausibly capable of accommodating other types of molecules.

1. INTRODUCTION

Molten salt synthesis via combinations of conventional ionic liquids and metal salts presents opportunities to tailor the physicochemical properties of the resulting compounds. This approach creates new metal-containing ionic liquid salts with unique properties. Conventional ionic liquids are salts with a melting temperature of <100 °C that usually contain large asymmetric organic cations and small inorganic anions with short-lived ion pairs. Ionic liquids are considered a class of "green compounds", which are currently receiving a lot of interest in various fields.[1−9] Metal-containing ionic liquids are a subclass of ionic liquids that combine the properties of the traditional ionic liquids with the unique chemical and/or physical properties of the incorporated metals. The introduction of metals greatly expands the possibilities of modification of ionic liquids, enabling their varied use in interdisciplinary applications.[3,10−16] The high thermal stability, negligible vapor pressures, and large liquidus range make ionic liquids attractive for a wide range of uses including as catalysts, magnetic

Received: August 26, 2021
Accepted: October 25, 2021
Published: November 16, 2021

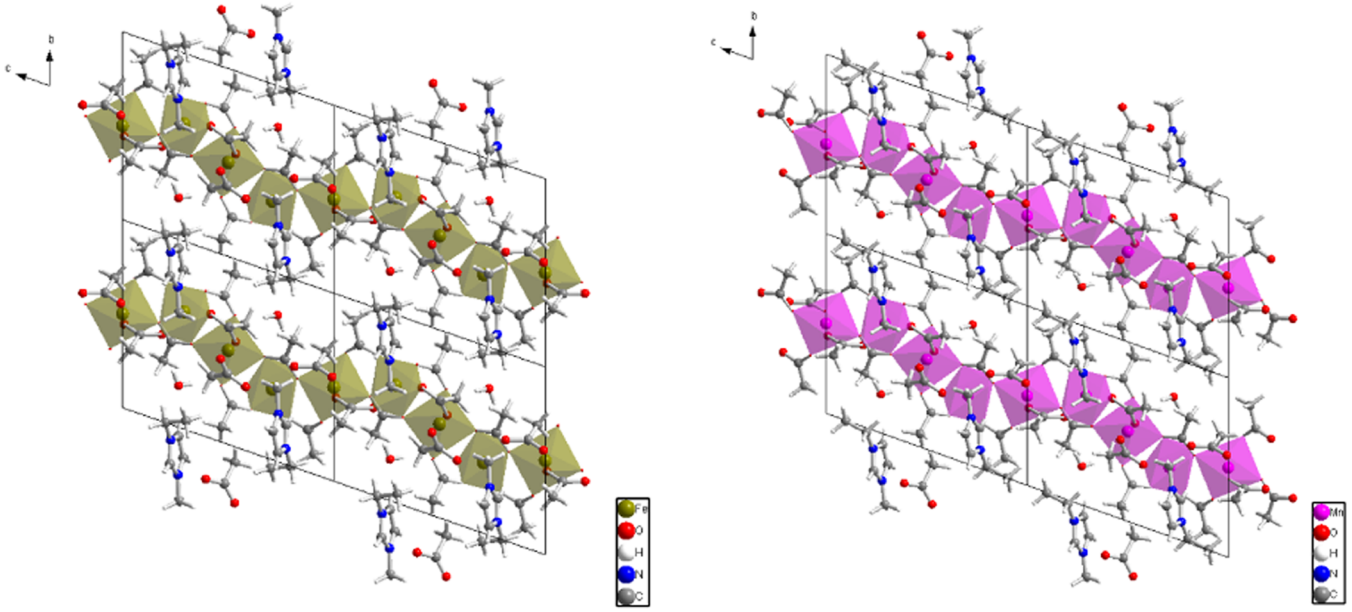

Figure 1. Crystal structure of compound **I** (left) viewed along the (100) crystallographic direction, compared with the isostructural Mn-based compound (right). The yellow and purple polyhedra represent Fe^{2+} and Mn^{2+} coordination environments, respectively. The chains of interconnected coordination polyhedra extend along the (001) direction.

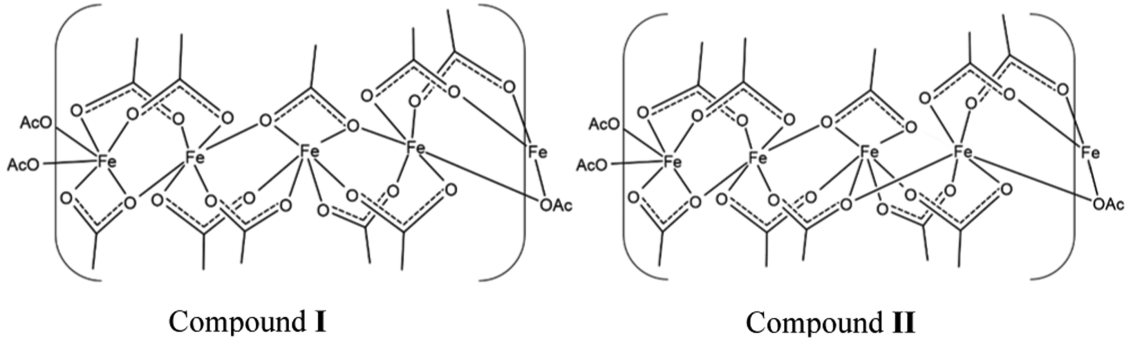

Figure 2. Schematic representation of the octahedral metal cation chain configuration in compounds **I** and **II**.

materials, electrolytes, and gas absorbers.[6−8,17−20] The technological performance of ionic liquids is determined by their structure and the dominant intermolecular forces. However, elucidating these properties in the liquid state is challenging due to the lack of periodicity; therefore, crystallographic characterization of frozen ionic liquids is one of the best ways to understand the ionic liquid structure.[21−24]

Ionic liquids have the potential to reversibly bind gases through a variety of intermolecular interactions.[5,6,8,25−27] The physical interaction of acid gas with ionic liquids is dependent on polarizability, dipole moments, and quadrupole moments, among other factors.[28] For most gases, solubility in conventional ionic liquids correlates well with polarizability, implying that gas solubility is dependent on dispersion forces and reorganization energies.[28] However, for acid gases (e.g., SO_2), quadrupole moments, as well as specific chemical interactions between the gas and the ionic liquid cation/anion, contribute to bonding; hence, multiple interactions can be utilized for the gas−ionic liquid binding.

1-Ethyl-3-methylimidazolium acetate, [EMIM][OAc], is one of the best-known ionic liquids.[5,29−31] Mixtures of [EMIM][OAc] with inorganic salts have also been reported to form ionic liquid materials.[32,33] Following a similar approach, we have explored the synthesis of other metal salts with [EMIM][OAc] in search of new metal-containing ionic liquids and molten salts for battery electrolytes and gas and water purification applications. We recently reported on the syntheses and characterization of the novel $Mn_4(OAc)_{10}[EMIM]_2$ and $Mn_4(OAc)_{10}[EMIM]_2{\cdot}2H_2O$ compounds featuring extended chains of octahedrally coordinated Mn^{2+} with all acetate ligands.[16] This paper reports the synthesis and characterization of the ambient crystalline material that was obtained by the thermal treatment of iron(II) acetate and [EMIM][OAc]. The material was characterized by X-ray diffraction (XRD), thermogravimetric analysis (TGA), differential thermal analysis (DTA), infrared, and temperature programmed desorption (TPD)-mass spectrometry (MS).

2. RESULTS AND DISCUSSION

2.1. X-ray Diffraction Studies. The chemical formulas of the hydrated and anhydrous salts, as determined from single-crystal X-ray diffraction experiments, are $C_{32}H_{56}Fe_4N_4O_{22}$ and $C_{32}H_{52}Fe_4N_4O_{20}$, which can be simplified as $Fe_4(OAc)_{10}[EMIM]_2{\cdot}2H_2O$ and $Fe_4(OAc)_{10}[EMIM]_2$. We will refer to these two salts as compounds **I** and **II** in this section. The as-synthesized product, anhydrous

https://doi.org/10.1021/acsomega.1c04670
ACS Omega 2021, 6, 31907−31918

$Fe_4(OAc)_{10}[EMIM]_2$, is highly hygroscopic. The hydrated product $Fe_4(OAc)_{10}[EMIM]_2{\cdot}2H_2O$ resulted from the absorption of moisture by some batches of the anhydrous product.

2.1.1. Compound I. $Fe_4(OAc)_{10}[EMIM]_2{\cdot}2H_2O$ is a dihydrate of $Fe_4(OAc)_{10}[EMIM]_2$. Like in the isostructural Mn-based analogue,[16] there are three symmetry-independent transition-metal cations in the unit cell of compound **I**. The metal cations form $[Fe3, Fe2, Fe3, Fe1]_n$ chains that extend along the (001) direction. As shown in Figure 1, all of the Fe^{2+} cations are octahedrally coordinated, and all six donor atoms are oxygens contributed by acetates. Fe3 has five nearest-neighbor acetates. Two acetates (C2, C4) are bidentate μ_2-1,3 bridging to Fe2, another two acetates (C8, C13) are bidentate μ_2-1,3 bridging to Fe1, whereas the last acetate (C6) in addition to bridging Fe2 and Fe1 is also chelating Fe3. Fe2 has six nearest-neighbor acetates. Four of the acetates (C2 and C4) are μ_2-1,3 bridging to Fe3. The other two acetates (C6) are bridging to Fe3 and chelating Fe3. Finally, Fe1 is coordinated by six acetates. Four of the acetates (C8 and C13) are μ_2-1,3 bridging to Fe3. The other two acetates (C6) are bridging to Fe3 and chelating Fe3. The coordination diagram of compound **I** is shown in Figure 2.

The crystal of compound **I** also contains only one symmetry-independent EMIM cation interacting with the acetate anions via van der Waals forces and C−H···O hydrogen bonds, as shown in Figure 3. In both anhydrous Mn-analog and dihydrate

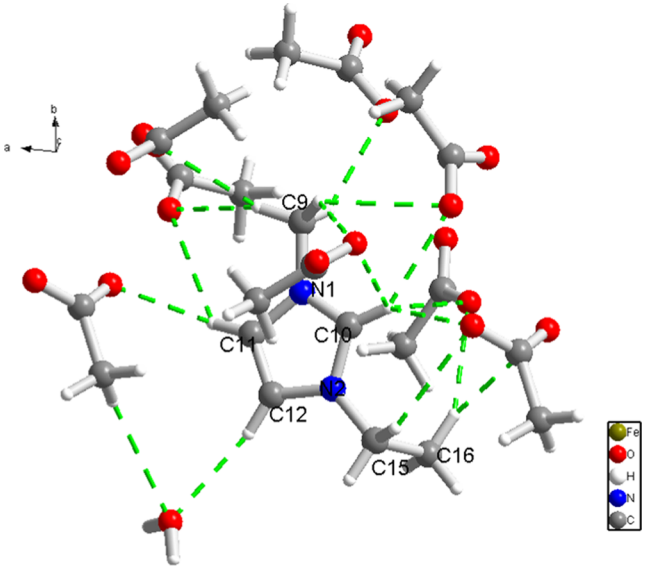

Figure 3. Hydrogen bonds (green dashed lines) connecting the EMIM cation, water molecule, and acetates in compound **I**.

Mn-analog compounds, the terminal hydrogens of the ethyl group of the EMIM moiety (H6A, H6B, and H6C in ah-Mn and H16A, H16B, and H16C for dh-Mn) were hydrophobic and did not take part in hydrogen bonding; however, this is not true for compound **I**, where the H16A hydrogen is located 2.572(9) Å from O7 and 2.89(1) Å from O3 and H15C is 2.76(1) Å from O2, all of which can be considered as weak hydrogen-bonding interactions. Each EMIM molecule is hydrogen-bonded with eight neighboring acetate ions and one water molecule. Each of the three EMIM aromatic hydrogens is connected via a hydrogen bond to an acetate oxygen, with H10 participating in four hydrogen bonds with O9, O2, O7, and O10. C6 methyl hydrogens are also all involved in hydrogen bonds. Geometric parameters of the hydrogen bonds are reported in the Supporting Information Table S9, and their arrangement is shown in Figure 3.

The arrangement of the metal cation chains and clustering of the methyl groups in compound **I** produce void spaces, available for guest species absorption. Automated search for structural cavities performed with the CrystalMaker program located the center of the structural void at fractional atomic coordinates (0.038131, 0.004213, −0.008040) and estimated the void radius at 2.584 Å, with a void volume of 72.307 $Å^3$, which is larger than the void in the dihydrate Mn compound, with a volume of 53.309 $Å^3$, despite the unit cell volume of dh-Fe being 7% smaller.

2.1.2. Compound II. Compound **II** contains three symmetry-independent transition-metal cations, connected in $[Fe2, Fe1, Fe2, Fe3]_n$ chains, oriented along the (001) direction. The crystal structure of compound **II** is different from the anhydrous Mn-analogue.[16] As shown in Figure 4, all of the Fe^{2+} cations are six-coordinated, and all six donor atoms are oxygens contributed by acetate ions. Fe2 has five nearest-neighbor acetates, similar to Fe3 in compound **I**. Two acetates (C12, C14) are bidentate μ_2-1,3 bridging to Fe1, another two acetates (C8, C16) are bidentate μ_2-1,3 bridging to Fe3, whereas the last acetate (C10), in addition to bridging Fe3 and Fe1 is also chelating Fe2. Fe1 is surrounded by six acetates and is similar to Fe2 in compound **I**. Four of the acetates (C12 and C14) are μ_2-1,3 bridging to Fe2. The other two acetates (C10) are bridging to Fe2 and chelating Fe2. Finally, Fe3 is coordinated by six acetates. Four of the acetates (C8 and C16) are μ_2-1,3 bridging to Fe3. The other two acetates (C6) are bridging to Fe2 and at the same time Fe1. As a result of this ligand configuration, neighboring Fe2 and Fe3 octahedra share the O1−O7 edge, whereas Fe2 and F1 only share the O6 corner. Edge sharing between neighboring transition-metal octahedral was not observed in the Mn analogues and is not present in Fe dihydrate. It results in a decrease of the interatomic distance between Fe2 and Fe3 to 3.26(3) Å compared to 3.591(4) Å between Fe1 and Fe2 across the shared octahedral corner. The distances between the neighboring transition-metal cations in the compound I, anhydrous Mn-analog and dihydrate Mn-analog compounds are also all longer than 3.5 Å due to the lack of edge sharing. Coordination diagram of compound **II** is shown in Figure 2.

As shown in Figure 5, the EMIM ions in compound **II** also do not participate in the coordination of the Fe cations but are hydrogen-bonded to the acetate anions. The EMIM moiety is hydrogen-bonded to nine acetate ions. The hydrogen of the ethyl group (H5B) is involved in two weak hydrogen bonds with O2 and O10. The geometric parameters of hydrogen bonds for compound **II** are reported in Supporting Information Table S10. Automated search for structural cavities in the compound **II** crystal structure, performed with the CrystalMaker program, located the center of the structural void at fractional atomic coordinates (0.275398, 0.277492, 0.566455) and estimated the void radius at 2.821 Å, with a void volume of only 94.12 $Å^3$, as compared to that of 117.4910 $Å^3$ in the anhydrous Mn salt. Compound **II** has a density of 1.496 g/cm^3, which is 4.3% higher than compound **I** (1.434 g/cm^3). We attribute this shrinkage of structural voids to the difference in ligand configuration around Fe cations and edge sharing of the FeO_6 octahedra.

Compounds **I** and **II** show structural arrangements resembling [EMIM][OAc]Cu(II) acetate/chloride,[33] in which the Cu ions form polyhedral chains (complexes **2** and **3**), with the disordered EMIM and H_2O molecules located in between

https://doi.org/10.1021/acsomega.1c04670
ACS Omega 2021, 6, 31907−31918

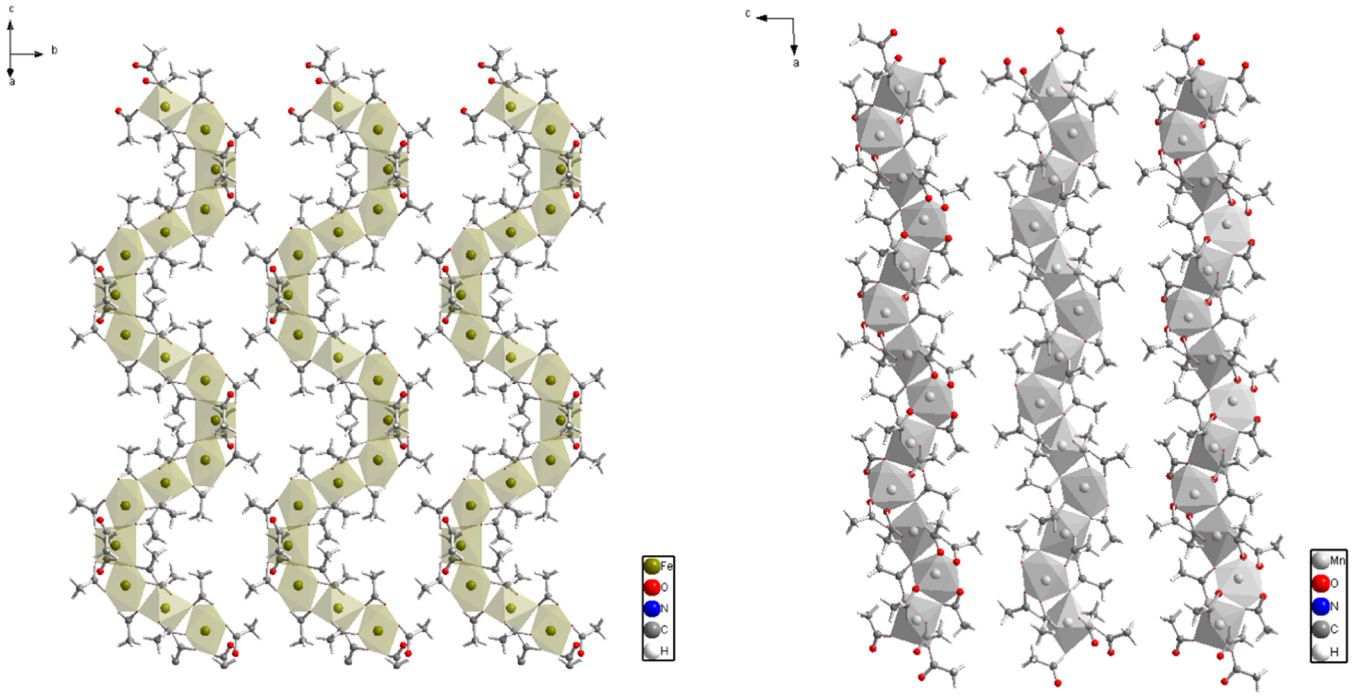

Figure 4. Arrangement of the metal cation polyhedral chain in compound **II** (left), viewed perpendicular to the chain direction compared with the isostructural Mn-based compound. EMIM ions are removed for clarity.

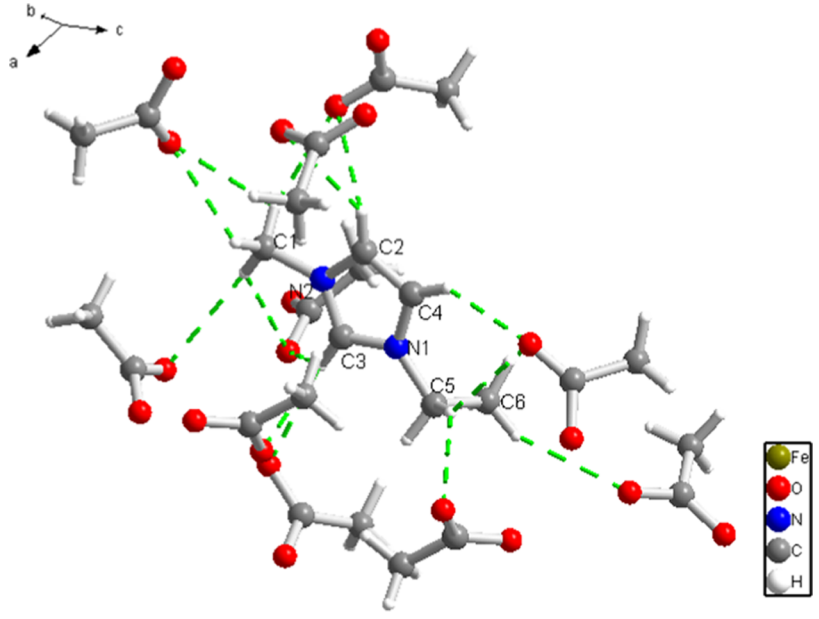

Figure 5. Hydrogen bonds (green dashed lines) connecting the EMIM cation and acetate anions in compound **II**.

the polyanionic chains. However, there is clustering of Cu ions involving Cu−Cu bonding, which is not observed in the two Fe compounds. The synthesized anhydrous $Fe_4(OAc)_{10}[EMIM]_2$ and the hydrated $Fe_4(OAc)_{10}[EMIM]_2{\cdot}2H_2O$ feature structural voids, as indicated in Figure 6. The void spaces may allow for the easy passage of gases through the bulk of the material and the binding of small gas contaminants (e.g., SO_2 and H_2S), making the materials potentially useful in separation and purification technologies. We envision that the careful selection of ionic liquid cation/anion and metal ion may lead to the optimum tuning of the void space size and shape, leading to selective and efficient gas sorptions.

The Rietveld refinement of the powdered sample was performed using the structure model of compound II, as determined in single-crystal experiments. The Rietveld refinement using the Bruker TOPAS 5 program converged to a final figure of merit R_{wp} = 4.029%. The sample was found to contain pure compound **II**; no traces of hydrated compound **I**, unreacted substrates, or other crystalline products were detected (Figure S1).

2.2. Fourier Transform Infrared (FTIR) Analyses. The FTIR spectrum of $Fe_4(OAc)_{10}[EMIM]_2$ is shown in Figure 7 compared with the spectra of the reactants, [EMIM][OAc] and $Fe(OAc)_2$. The spectrum of the new $Fe_4(OAc)_{10}[EMIM]_2$

https://doi.org/10.1021/acsomega.1c04670
ACS Omega 2021, 6, 31907−31918

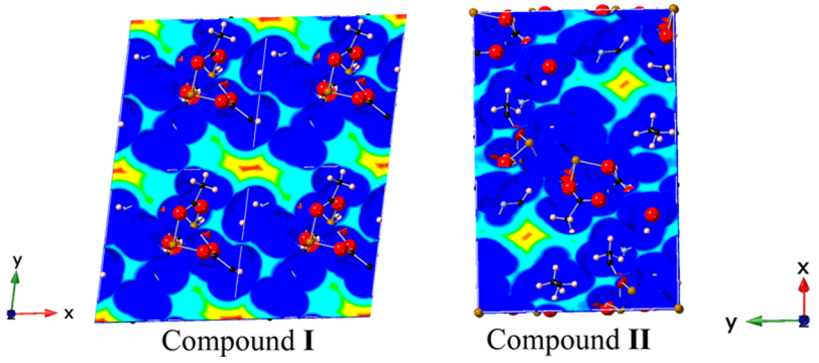

Figure 6. Van der Waals distance maps for compounds **I** and **II**, showing structural void space available for absorption.

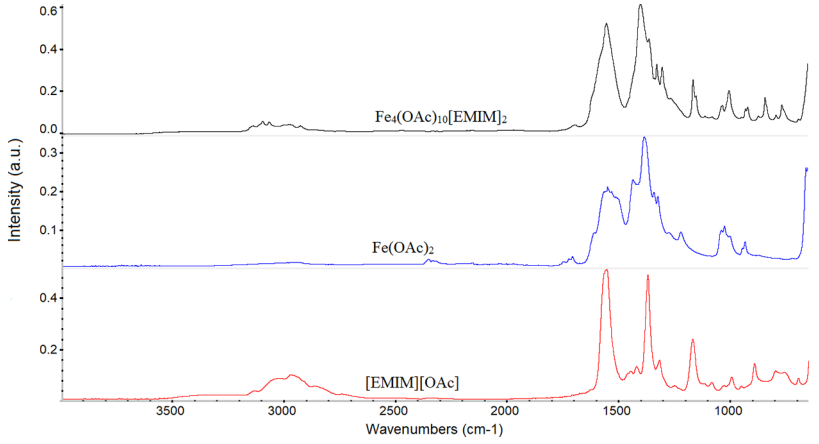

Figure 7. Room-temperature FTIR spectra of $Fe_4(OAc)_{10}[EMIM]_2$, $Fe(OAc)_2$, and [EMIM][OAc].

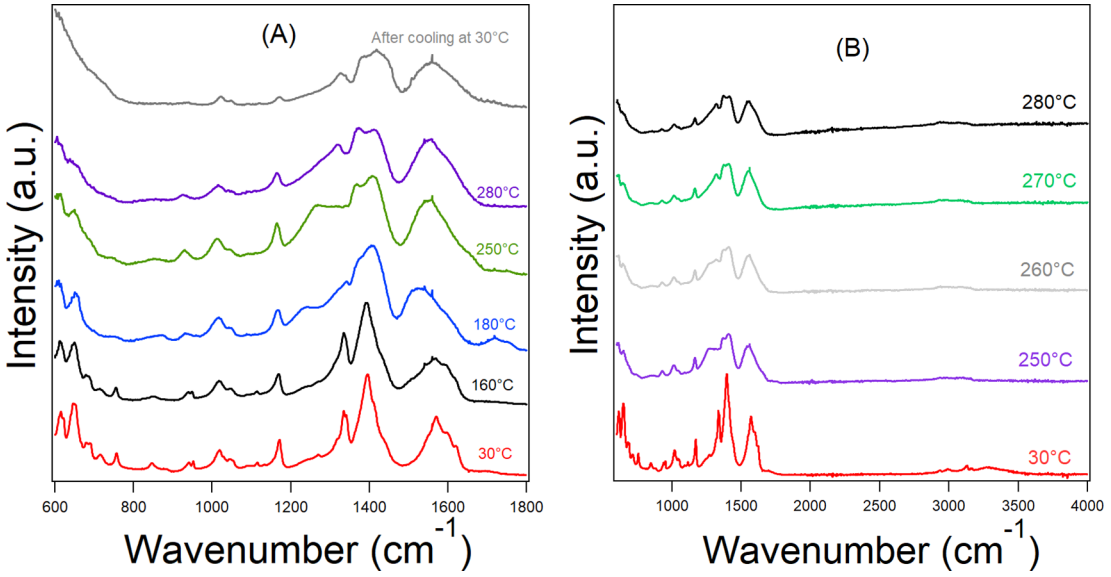

Figure 8. FTIR spectra of $Fe_4(OAc)_{10}[EMIM]_2$ at various temperatures: (A) 30−280 °C and after cooling to 30 °C in the 600−1800 cm^{-1} region and (B) 30−280 °C in the 600−4000 cm^{-1} region.

compound shows the following frequencies at 755 cm^{-1} (CC stretching + OCO bending), 846 cm^{-1} (CC stretching + OCO bending), 944 cm^{-1} (CH_3 bending), 1170 cm^{-1} (in-plane $C_{Im}H$ bending), 1042 cm^{-1} (CH_3 bending), 1334 cm^{-1} (symmetric CO stretching), 1393 cm^{-1} (CH_3 bending), 1568 and 1569 cm^{-1} (antisymmetric CO stretching), and 613 and 644 cm^{-1} (OCO bending + CC stretching).[34−40] For $Mn_4(OAc)_{10}[EMIM]_2$, bands at 761 and 844 cm^{-1} were assigned to the Mn-acetate chains in that structure.[16] The signal at 1618 cm^{-1} may indicate the presence of the coordination of the acetate ion with Fe^{2+} through the oxygen atoms. The infrared modes of the ionic liquid [EMIM][OAc] are in agreement with the literature and are reported as follows: 630 cm^{-1} (CC stretching + OCO bending), 896 cm^{-1} (CC stretching + OCO

https://doi.org/10.1021/acsomega.1c04670
ACS Omega 2021, 6, 31907−31918

bending), 995 and 1035 cm^{-1} (CH_3 bending), 1322 cm^{-1} (symmetric CO stretching), 1373 and 1425 cm^{-1} (CH_3 bending), 1567 cm^{-1} (antisymmetric CO stretching), 702 cm^{-1} (in-plane ring deformation + $C_{Me}N$ stretching + $C_{Et}N$ stretching), and 1171 cm^{-1} (in-plane $C_{Im}H$ bending).[41,42] The IR spectrum of $Fe(OAc)_2$ agrees with the findings of Edwards et al.[40] and shows the following frequencies: 1558 cm^{-1} (antisymmetric CO stretching), 1402 cm^{-1} (antisymmetric CO stretching), 1366 cm^{-1} (CH_3 bending), 1039 cm^{-1} (CH_3 bending), 1010 cm^{-1} (CH_3 bending), 941 cm^{-1} (CC stretching), and 928 cm^{-1} (CC stretching).

The $Fe_4(OAc)_{10}[EMIM]_2$ was further investigated by variable-temperature FTIR to determine the effect of temperature on the molecular bonding and stability of the compound. Hence, the material was heated in the temperature range of 30−280 °C, with spectra collected at every 10 °C interval, as shown in Figure S2 in the Supporting Information. Then, the sample was cooled down to 30 °C and another spectrum was collected. The IR spectra of the $Fe_4(OAc)_{10}[EMIM]_2$ at 30, 160, 180, 250, 280 °C, and after cooling to 30 °C are displayed in Figure 8. A phase transition of the compound is observed in the temperature range of 160−180 °C (see Section 2.3) where the peak at 755 cm^{-1} disappears (see Figure 8A), as well as the weaker bands at 670 and 710 cm^{-1}. The band at 846 cm^{-1} broadens strongly in this temperature range. Further, the signals at 1334 and 1393 cm^{-1} are merged into a broad peak, which may indicate the formation of a liquid phase of $Fe_4(OAc)_{10}[EMIM]_2$. These signals are attributed to the vibrational modes of the acetate ion, which might indicate that a change of the orientation of the acetate ion occurs leading to a lower interaction with the $[EMIM]^+$ before the onset of decomposition of the acetate. Between 180 and 250 °C, a broad band grows at around 1300 cm^{-1} and disappears above 250 °C.

A comparison between the IR spectra collected at 30 °C before heating and after cooling the sample is shown in Figure 8, in which the disappearance of the acetate anion signals at 755, 846, and 944 cm^{-1} after cooling suggests that the complex is decomposed during the heating process. Figure S3 shows the decrease of the intensity of the absorption bands of $Fe_4(OAc)_{10}[EMIM]_2$, which may correspond to the dissociation into the starting compounds. One observes also the decrease of the band at around 1300 cm^{-1}, which has appeared upon heating from 180 to 250 °C, as shown in Figure 8. The origin of this band is not clear. Figure S4 shows that between 270 and 280 °C, mainly [EMIM][OAc] is decomposed, and after heating to 280 °C, mainly $Fe(OAc)_2$ remains, as illustrated in Figure S5. There is still a small amount of [EMIM][OAc] after heating to 280 °C, as seen by the small peak at 1170 cm^{-1} for this sample (see Figures S4 and S5).

The FTIR spectrum of $Mn_4(OAc)_{10}[EMIM]_2$ has been published recently.[16] The authors found that all Mn^{2+} ions are six-coordinated, and the donor atoms are the oxygens of the acetates, while the $EMIM^+$ ions interact through the van der Waals interaction and C−H−O hydrogen bonds with the acetate ligand. The IR spectra of $Fe_4(OAc)_{10}[EMIM]_2$ and $Mn_4(OAc)_{10}[EMIM]_2$ show similar features displayed in Figure 9, which is in line with the similarities in their XRD structure. The broad band at 3300−3360 cm^{-1} could be ascribed to N−H or O−H subject to hydrogen bonding.

2.3. TGA and DTA. Thermogravimetric analysis (TGA) and differential thermal analysis (DTA) were performed to elucidate the thermal properties of the $Fe_4(OAc)_{10}[EMIM]_2$ on heat treatment from 50 to 600 °C. TGA indicates about 72 wt % mass loss of the material (Figure 10). The majority of the weight loss occurs in multiple overlapping steps in the 245−350 °C temperature range, unlike the iron acetate reactant that decomposes through a well-defined three-step process while losing 62 wt % of its mass between 200 and 450 °C. The TGA result supports the VT-IR analyses, which suggests decomposition of the $Fe_4(OAc)_{10}[EMIM]_2$ complex upon heating to 280 °C. The [EMIM][OAc] ionic liquid is observed to decompose in a single step around 245 °C, with almost complete volatilization of the decomposed products.[16,43] The $Fe_4(OAc)_{10}[EMIM]_2$ is more thermally stable compared to [EMIM][OAc] but less stable than the iron acetate. The observed higher thermal stability of the $Fe_4(OAc)_{10}[EMIM]_2$ ionic liquid is likely due to increased lattice ordering and ionic bonding relative to [EMIM][OAc]. This high thermal stability

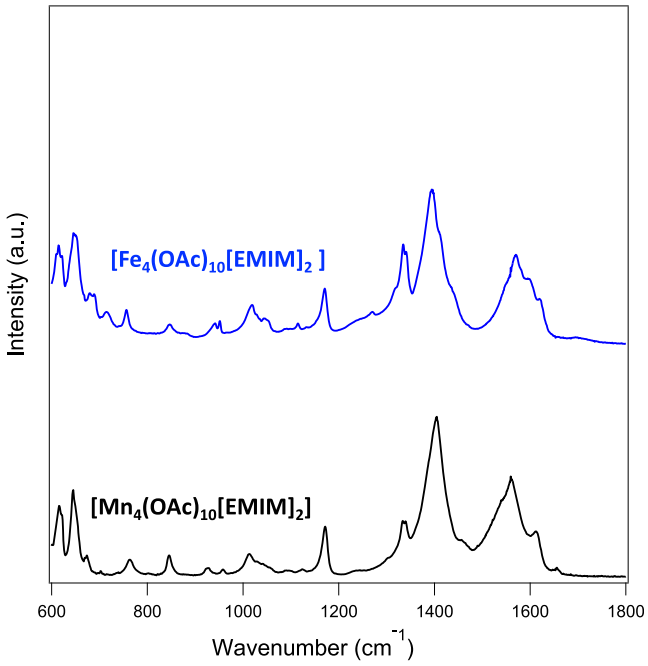

Figure 9. Comparison of FTIR spectra of the $[Mn_4(OAc)_{10}[EMIM]_2]$ and $Fe_4(OAc)_{10}[EMIM]_2$ collected at 30 °C.

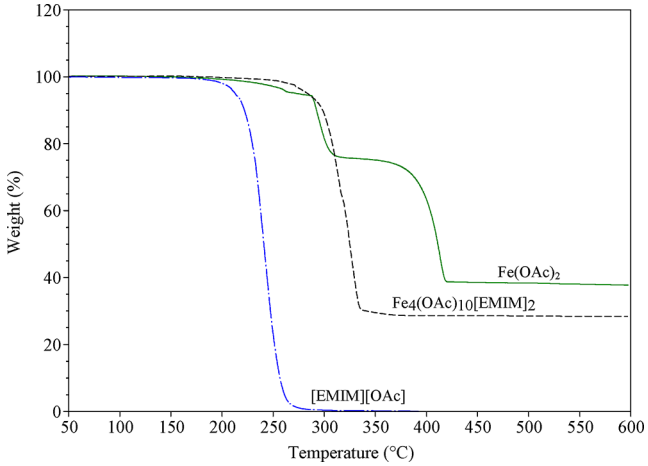

Figure 10. Thermogravimetric analyses of [EMIM][OAc], $Fe(OAc)_2$, and $Fe_4(OAc)_{10}[EMIM]_2$ at 10 °C/min under an Ar flow.

https://doi.org/10.1021/acsomega.1c04670
ACS Omega 2021, 6, 31907−31918

was also observed with the $Mn_4(OAc)_{10}[EMIM]_2$ compounds.[16]

The TGA spectra of all of the $Fe_4(OAc)_{10}[EMIM]_2$ samples do not show the 3 wt % mass loss at a lower temperature (<150 °C), which could be attributed to the two absorbed water molecules seen in the hydrated $Fe_4(OAc)_{10}[EMIM]_2$ by XRD analyses. The observance of negligible weight loss suggests that the anhydrous $Fe_4(OAc)_{10}[EMIM]_2$ is highly hygroscopic and may have absorbed the moisture during sample handling for other characterization, hence the determination of $Fe_4(OAc)_{10}[EMIM]_2{\cdot}2H_2O$ and $Fe_4(OAc)_{10}[EMIM]_2$ from different batches of samples by XRD. This scenario is highly likely as anhydrous materials were utilized in syntheses and the samples were prepared under an Ar atmosphere and stored in a glovebox.

The DTA thermogram of $Fe_4(OAc)_{10}[EMIM]_2$ (Figure 11) shows four endothermic peaks with maxima at 108, 157, 296

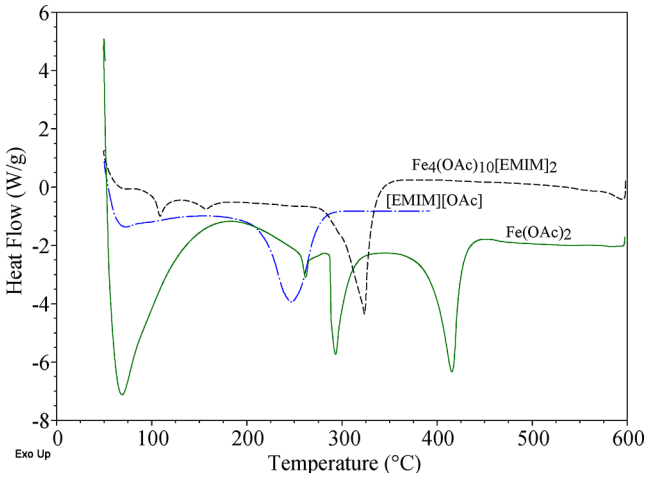

Figure 11. Differential thermal analysis of [EMIM][OAc], $Fe(OAc)_2$, and $Fe_4(OAc)_{10}[EMIM]_2$ at 10 °C/min under an argon flow.

(shoulder), and 324 °C. The endothermic peaks at 296 and 324 °C are attributed to the decomposition of the $Fe_4(OAc)_{10}[EMIM]_2$, plausibly to iron oxides. The peak at 157 °C is likely associated with structural rearrangement in $Fe_4(OAc)_{10}[EMIM]_2$. This thermal event is observed in VT-IR at around 160−180 °C as a disappearance of the vibrational peak at 755 cm^{-1}. The peak with the maximum intensity at 108 °C is due to the melting of the $Fe_4(OAc)_{10}[EMIM]_2$. The onset melting temperature of the $Fe_4(OAc)_{10}[EMIM]_2$ was determined at a slower heating rate of 1 °C/min, as shown in Figure S6. The extrapolated onset melting point of the $Fe_4(OAc)_{10}[EMIM]_2$ was found to be ∼94 °C. However, due to the broadness of the melting transition, the extrapolated onset temperature was deemed less reliable; hence, the melting equilibrium was visually determined with an SRS Digimelt apparatus, which showed an onset of melting temperature between 92 and 96 °C. At this lower heating rate, the decomposition of the $Fe_4(OAc)_{10}[EMIM]_2$ could also be clearly deconvoluted into two main peaks, plotted in Figure S6. The presence of the two well-defined peaks supports the FTIR analyses (Figures S3−S5), indicating the dissociation of the $Fe_4(OAc)_{10}[EMIM]_2$ during decomposition into the starting materials (eq 1) with concomitant loss of the formed [EMIM][OAc] followed by the iron acetate species. Similar decomposition pathways have been previously reported for other double-cation compounds[44,45]

$$Fe_4(OAc)_{10}[EMIM]_2 \xrightarrow{240-280\,^{\circ}C} 2[EMIM][OAc] + 4Fe(OAc)_2 \quad (1)$$

The $Fe_4(OAc)_{10}[EMIM]_2$ and $Mn_4(OAc)_{10}[EMIM]_2$ have relatively similar thermal stabilities (Figure 12).[16] Both Fe and

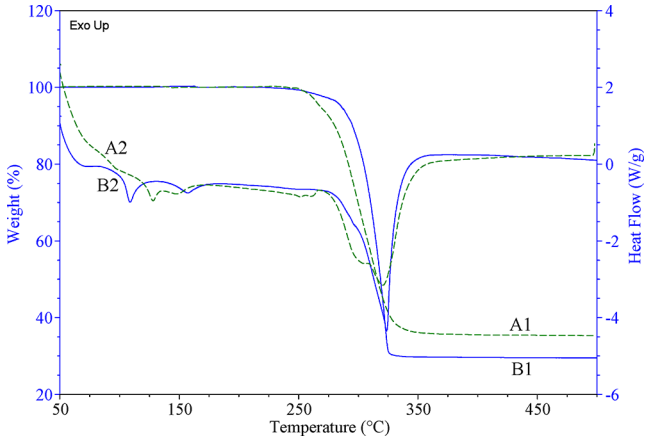

Figure 12. Comparison of TGA (1) and DTA (2) spectra at 10 °C/min under an argon flow of $Mn_4(OAc)_{10}[EMIM]_2$ (A) and $Fe_4(OAc)_{10}[EMIM]_2$ (B).

Mn compounds decompose within a 240−350 °C temperature range. The similarity in thermal stability is attributed to the structural resemblance of the Mn and Fe dicationic compounds, as observed in the X-ray diffraction and vibrational spectroscopy studies. However, differences in the two compounds are also observed; for instance, the Fe compound has a lower melting point compared to the Mn compound. The subtle differences could be due to differences in electronegativity and covalency of transition-metal ions. The changing of the metal ion (size, type, or charge) is envisioned to further alter the physicochemical properties of the metal-containing ionic liquids resulting in new materials with unique properties.

2.4. Decomposition of $Fe_4(OAc)_{10}[EMIM]_2$ from Temperature Programmed Desorption. The gas-phase products liberated during the temperature-programmed desorption of $Fe_4(OAc)_{10}[EMIM]_2$ were monitored by means of quadrupole mass spectrometry (QMS) up to 450 °C (Figure 13). The ions at m/z = 15, 18, 28, 43, 45, 58, and 74 were assigned to the molecules CH_3, H_2O, N_2 and CO, OC−CH_3, OH−CO, H_3C−CO−CH_3, and H_3CO−CO−CH_3, respectively. These m/z-values represent the key species involved in the thermal decomposition of $Fe_4(OAc)_{10}[EMIM]_2$. The decomposition pathway of the $Fe_4(OAc)_{10}[EMIM]_2$ involves four distinct regimes with peak temperatures of 88, 200, 267, and 345 °C. The first regime is associated with the release of absorbed H_2O, as observed by XRD in hydrated $Fe_4(OAc)_{10}[EMIM]_2$.

The second regime is associated with the decomposition of a majority of the [EMIM] cation[43,46−48] in the temperature range of 180−230 °C and the onset loss of the acetate anions coordinated to the Fe(II) cation. The release of [EMIM] cation volatile decomposition products (e.g., 1-methylimidazole (m/z = 82) or 1-ethylimidazole (m/z = 96)) is largely overwhelmed by species related to the acetate anion decomposition (OC−CH_3 and OH−CO); hence, no clear fragmentation pattern from

https://doi.org/10.1021/acsomega.1c04670
ACS Omega 2021, 6, 31907−31918

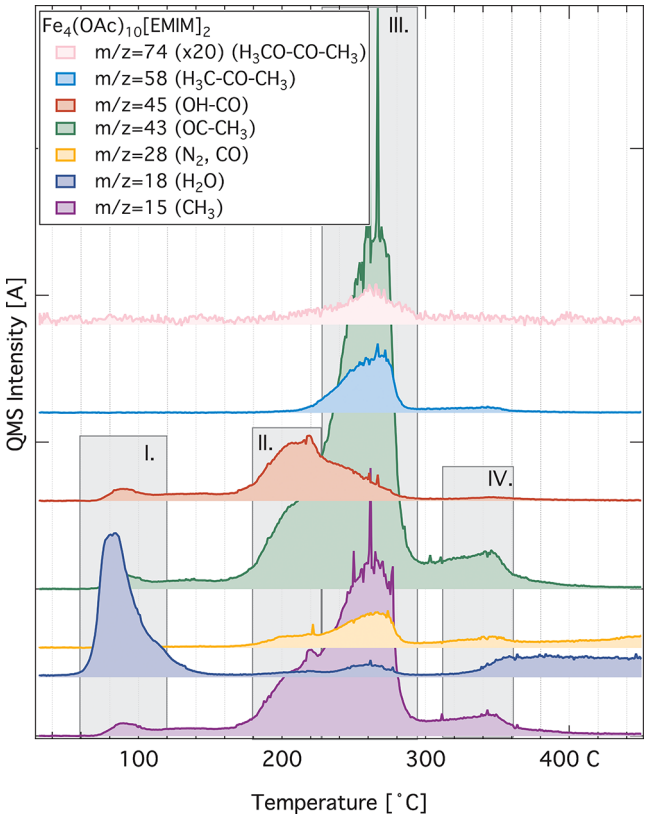

Figure 13. Evolution of the selected m/z recorded by quadrupole mass spectrometry during the temperature-programmed desorption of $Fe_4(OAc)_{10}[EMIM]_2$ in the temperature range of 30−450 °C heated at 10 °C/min. The signal of m/z = 74 was multiplied by 20 for clarity.

the imidazolium cation can be identified, as similarly observed by Clough et al.[43] in TGA-MS decomposition of imidazolium ionic liquids. The major loss of the [EMIM] moiety is aligned with XRD results, which indicate a weak bonding interaction of the [EMIM] cations to the central $Fe_4(OAc)_{10}$ moiety. The decomposition of the [EMIM] cation is envisioned to lead to the loss of charge balance in $Fe_4(OAc)_{10}[EMIM]_2$, resulting in the observed concomitant loss of some of the acetate anions at the same temperatures to balance the charge. To further understand the release and fragmentation of [EMIM] and [OAc] ions, we attempted to study the decomposition of the [EMIM][OAc] reactant. However, in line with King et al.,[47] we observed a slow distillation of the [EMIM][OAc] on exposure to the high vacuum of the TPD-mass spectrometer; hence, we could not analyze the sample due to the instrument's incompatibility with liquids. Clough et al.[43] reported the formation of methyl acetate and ethyl acetate as major fragments of the decomposition of [EMIM][OAc], using TGA-MS analyses, as well as 1-methylimidazole and 1-ethylimidazole detected by NMR, indicative of mostly S_N2 decomposition mechanism. The products of $Fe_4(OAc)_{10}[EMIM]_2$ fragmentation suggest the predominance of multiple decomposition mechanisms. The release of acetic acid ($HO-CO-CH_3$) m/z = 60 (Figure S7a) and its fragmentation products represented by both m/z = 43 ($OC-CH_3$) and 45 ($OH-CO$) is indicative of heterocyclic carbene or E2 Hofmann elimination decomposition mechanisms.

In the third regime, 230−290 °C, most of the acetate ions are released as evidenced by the marked increase of m/z = 43 (H_3C-CO), m/z = 58 ($H_3C-CO-CH_3$), and m/z = 74 ($H_3C-O-CO-CH_3$). The m/z = 74 species is assigned to methyl acetate formed through the S_N2 reaction mechanism from the concurrent decomposition of the acetate or acetyl bound to Fe^{2+} and the residual methyl group of methylimidazole species. The presence of the $H_3C-CO-CH_3$ fragment suggests similarities in acetate fragmentation in regime III of $Fe_4(OAc)_{10}[EMIM]_2$ to that of $Fe(OAc)_2$ with the formation of iron oxides.[48] Regime four is likely predominated by the formation of Fe_3O_4 and its transition to Fe_2O_3. The decomposition temperature profile of the $Fe(OAc)_2$ is different from that of $Fe_4(OAc)_{10}[EMIM]_2$. Three main decomposition regimes can be identified (Figure 14), with peak temperatures of

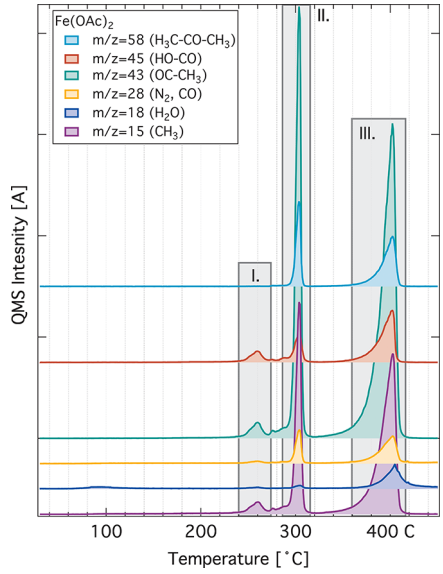

Figure 14. Evolution of the selected m/z recorded by quadrupole mass spectrometry during the temperature-programmed desorption of $Fe(OAc)_2$ in the temperature range of 30−450 °C heated at 10 °C/min.

260 °C, 304 °C, and 402 °C, respectively. These regimes coincide with the multistep decomposition from TGA and DTA results shown in Figure 11. All three decomposition steps involve the release of acetic acid m/z = 60 ($HO-CO-CH_3$), represented by both m/z = 43 and 45. Based on the literature reports,[49,50] we propose that the three-step decomposition mechanism of the $Fe(OAc)_2$ involves the formation of Fe_2O_3 and Fe_3O_4, which is subsequently rearranged into Fe_2O_3. Elmasry et al.[49] reported on the decomposition of hydrated $Fe(OAc)_2$, which is different from the anhydrous $Fe(OAc)_2$ reported herein. The concomitant hydrolysis of the hydrated $Fe(OAc)_2$ could accelerate the decomposition process and thereby explain the lower decomposition temperatures and the seemingly one-step pathway reported.[49]

2.5. CONCLUSIONS

In this work, we synthesized and characterized a novel iron(II) aceto EMIM compound with the empirical formula $Fe_4(OAc)_{10}[EMIM]_2$ and determined the crystal structure in two different hydration forms: an anhydrous monoclinic compound and a triclinic dihydrate, $Fe_4(OAc)_{10}[EMIM]_2 \cdot 2H_2O$. The dihydrate is formed by the absorption of moisture by the highly hygroscopic anhydrous compound. The dihydrate compound is isostructural, with the recently reported $Mn_4(OAc)_{10}[EMIM]_2 \cdot 2H_2O$, while the anhydrate is a superstructure of the Mn counterpart, suggesting the existence of solid

https://doi.org/10.1021/acsomega.1c04670
ACS Omega 2021, 6, 31907−31918

solutions. Both compounds contain chains of Fe^{2+} octahedrally coordinated exclusively by acetate groups. The EMIM moieties do not directly interact with the iron cation and contribute to the structural framework of the compound through hydrogen bonding with the acetate anions. The $Fe_4(OAc)_{10}[EMIM]_2$ has a melting temperature of ~94 °C and can therefore be considered as metal-containing ionic liquids. Thermal analysis using DTA and VT-IR suggests structural rearrangement in the molten state taking place around 150−180 °C. Thermogravimetric analyses indicate about 72 wt % mass loss at 250−325 °C. The $Fe_4(OAc)_{10}[EMIM]_2$ compounds are more thermally stable than their Mn counterparts and [EMIM][OAc] but have lower stability compared to iron acetate. TPD coupled with quadrupole mass spectrometry shows the main species in the decomposition of $Fe_4(OAc)_{10}[EMIM]_2$ with peak temperatures at 88, 200, 267, and 345 °C to be CH_3, H_2O, N_2 and CO, OC−CH_3, OH−CO, H_3C−CO−CH_3, and/or H_3C−O−CO−CH_3. The structural arrangement represented by the $Fe_4(OAc)_{10}[EMIM]_2$ compounds is porous and may be capable of accommodating other types of molecules. The metallo-ionic liquids may offer an opportunity to further tune gas-binding interactions into the reversible regime necessary for gas storage, separation, or purification.

3. EXPERIMENTAL SECTION

3.1. Materials. The 1-ethyl-3-methylimidazolium acetate ([EMIM][OAc]) ionic liquid, 97% (Sigma-Aldrich), and iron(II) acetate powder, anhydrous (Alfa Aesar), were stored in an argon (Ar)-filled glovebox. The ionic liquid was initially vacuum-dried for 12 h at 90 °C prior to use.

3.2. Synthesis Procedure. The novel iron(II) materials were prepared using a solvent-free synthesis method, as reported previously.[16] In short, the anhydrous iron(II) acetate (1.04 g, 6.0 mmol) was mixed with the vacuum-dried, 1-ethyl-3-methylimidazolium acetate (0.51 g, 3.0 mmol) ionic liquid at a 2:1 molar ratio, respectively. Upon mixing at room temperature, a blackish-brown solid product was observed. The mixture was heated to about 110 °C with stirring for 2 h under an inert Ar atmosphere. The viscous product was slowly cooled with concomitant solidification to room temperature. Upon standing at room temperature for at least 24 h, the product turned light brown and then pinkish-brown on crushing the solid product. Alteration of the iron(II) acetate and ionic liquid ratios resulted in the same product being formed and residual starting materials. The solid product was stored in the Ar glovebox for further characterization. The as-synthesized product, anhydrous $Fe_4(OAc)_{10}[EMIM]_2$, is highly hygroscopic. The hydrated product $Fe_4(OAc)_{10}[EMIM]_2{\cdot}2H_2O$ resulted from the absorption of moisture by some batches of the anhydrous product. Consequently, the anhydrous $Fe_4(OAc)_{10}[EMIM]_2$ parent product was characterized by FTIR, TGA, DTA, and TPD, while the anhydrous and hydrated versions of the $Fe_4(OAc)_{10}[EMIM]_2$ were elucidated by XRD.

3.3. XRD Techniques. The synthesized solid product was loaded into a glass capillary, which was then sealed with vacuum grease under a nitrogen (N_2) atmosphere. The X-ray diffraction data were measured on a Bruker D8 Venture diffractometer equipped with an Incoatec IμS 3.0 Ag Kα source (λ = 0.56086 Å), a Helios focusing optics, a 3-circle, fixed-chi goniometer, and a Photon II detector. The total exposure time for each data collection was approximately 6 h. The integration of diffraction images was performed with the Bruker SAINT software package. The chemical formulas of the two compounds, as determined from the single-crystal X-ray diffraction experiments, are $C_{32}H_{56}Fe_4N_4O_{22}$ and $C_{32}H_{52}Fe_4N_4O_{20}$, which can be expressed as $Fe_4(OAc)_{10}[EMIM]_2{\cdot}2H_2O$ and $Fe_4(OAc)_{10}[EMIM]_2$ and will be referred to as compounds **I** and **II**, respectively. For compound **I**, the integration of the data produced a total of 17 333 reflections to a maximum θ angle of 20.18° (0.81 Å resolution), of which 4216 were independent (average redundancy 4.111, completeness = 97.81%, R_{int} = 15.41%, R_{sig} = 14.10%) and 2569 (60.93%) were greater than $2\sigma(F^2)$. The limited completeness of the data was a consequence of restricted rotations of the sample mounted in a long capillary and difficulty with centering the sample, surrounded by other crystals inside the capillary. The final cell constants of a = 9.0333(13) Å, b = 10.5505(15) Å, c = 12.4384(18) Å, α = 70.784(5)°, β = 88.387(6)°, γ = 81.848(6)°, and volume = 1107.9(3) Å^3 are based upon the refinement of the *XYZ*-centroids of reflections above $20\sigma(I)$. The calculated minimum and maximum transmission coefficients (based on crystal size) are 0.6863 and 0.8350 and are very similar to the values obtained for $Mn_4(OAc)_{10}[EMIM]_2{\cdot}2H_2O$.[16] The unit cell volume of the Fe compound is 6.6% smaller than the Mn compound, and its density is 7.4% higher due to the difference in molecular mass. Absorption correction was applied using the multiscan method (SADABS). The ratio of the minimum-to-maximum apparent transmission was 0.911. The calculated minimum and maximum transmission coefficients were 0.6779 and 0.7444, respectively. The crystal structure of compound **I** was solved and refined using the Bruker SHELXTL software package, in space group $P\bar{1}$, with Z = 2 for the formula unit $C_{16}H_{28}Fe_2N_2O_{11}$. For simplicity of comparison, the atom names for the Fe compounds were assigned following the same convention as for the isostructural Mn compound.[16] The final anisotropic full-matrix least-squares refinement on F^2 with 298 variables converged at R_1 = 10.64% for the observed data and wR_2 = 23.03% for all data. The goodness-of-fit was 1.083. The maximum peak in the difference electron density map was 1.200 e/Å^3, and the largest hole was −0.642 e/Å^3. On the basis of the final structure model, the calculated density was 1.607 g/cm^3 and F(000), 556 e. Constraints AFIX 137 were used to refine idealized riding hydrogen positions in methyl groups of the EMIM cation carbon atoms C9 and C16 and acetate carbon atoms C1, C3, C5, C7, and C14. Hydrogen atoms connected to C10, C11, and C12, the three aromatic carbons of the EMIM cation, were refined with AFIX 43 constraints, as idealized riding aromatic C−H. Hydrogen atoms connected to the C15 atom of the EMIM moiety were also refined using constraints with AFIX 23, as idealized riding secondary CH2. No disorder was observed in compound **I**. For compound **II**, the integration of the data produced a total of 8419 reflections to a maximum θ angle of 18.15° (0.90 Å resolution), of which 3105 were independent (average redundancy 2.711, completeness = 95.1%, R_{int} = 11.00%, R_{sig} = 12.41%) and 1919 (61.80%) were greater than $2\sigma(F^2)$. The final cell constants of a = 25.893(17) Å, b = 12.764(9) Å, c = 18.520(12) Å, β = 132.228(17)°, and volume = 4532.(5) Å^3 are based on the refinement of reflections above $20\sigma(I)$. The structure of compound **II** was solved and refined in a similar way as described above and was found to be different from the Mn anhydrous counterpart. The space group was determined to be $C2/c$, with Z = 8 for formula unit $C_{16}H_{26}Fe_2N_2O_{10}$, as compared to Z = 4 for the Mn anhydrous compound. The final anisotropic full-matrix least-squares refinement on F^2 with 280 variables converged at R_1 = 7.60% for the observed data and wR_2 = 24.50% for all data. The

https://doi.org/10.1021/acsomega.1c04670
ACS Omega 2021, 6, 31907−31918

goodness-of-fit was 1.075. The largest peak in the final difference electron density synthesis was 1.01 e/Å^3, and the largest hole was −0.67 e/Å^3. The calculated density was 1.519 g/cm^3 and $F(000)$, 2144 e. Details of the crystallographic refinement statistics and final structural parameters for compounds **I** and **II** are included in the Supporting Information, Tables S1−S8. To constrain the yield and purity of the synthesis, an additional powder X-ray diffraction experiment was conducted on the as-synthesized, anhydrous product, sample II. The loading of the sample into an airtight-domed container with a zero-background Si wafer plate was done inside an argon glovebox. The diffraction measurements were performed using a Bruker D8 Advance diffractometer equipped with a LynxEye XE detector and a Cu Kα X-ray source operating at 40 keV and 40 mA. Data acquisition was performed over an angular range from 5 to 45°, with a step of 0.01° and an acquisition time of 1 second per step. During the data collection, the sample was rotated at an angular speed of 15 rpm.

3.4. FTIR Analyses. The attenuated total reflection Fourier transform infrared (ATR-FTIR) analyses of the reactants and products were performed at room temperature using a Nicolet iS10 ATR infrared spectrometer equipped with a diamond crystal located outside a glovebox, under a N_2 purge of sample and diamond crystal. The spectra were collected at a resolution of 4 cm^{-1} with 64 scans per sample in the range 650−4000 cm^{-1}. Variable-temperature (VT) FTIR analyses were done using a Biorad Excalibur Instrument with a portable Specac Golden Gate heatable ATR setup, which allowed for sample preparation in the glovebox. The samples were heated from 30 to 280 °C with a step of 10 °C. Then, the IR was collected after cooling down the samples at 30 °C. The VT-IR spectra were collected in the range 600−4000 cm^{-1}at a resolution of 2 cm^{-1} with 30 scans.

3.5. TGA and DTA. Thermogravimetric analysis (TGA) and differential thermal analysis (DTA) of materials were performed on a Q600 SDT from TA Instruments utilizing a temperature ramp of 10 °C/min under an Ar flow of 100 mL/min at 50−600 °C. About 5−10 mg of material was sealed in perforated Tzero aluminum pans and utilized in each of the thermal experiments.

3.6. Temperature Programmed Desorption Coupled with Mass Spectrometry. In a custom-built thermal-programmed desorption setup coupled with quadrupole mass spectrometry (TPD-QMS),[51] the materials were heated from 26 to 450 °C at 10 °C/min using a Digi-Sense temperature controller. The gas-phase species released during heating were analyzed by the residual gas analyzer (RGA) Stanford Research Systems RGA 100 at a 70 eV ionization energy, scanning m/z = 1−100 amu at a sampling rate of 4 s. A LabVIEW interface controlled all of the experimental parameters. The samples were each packaged in platinum foil to ensure homogeneous heating over the entire sample and were subsequently placed in a quartz tube that was mounted to the TPD system. The quartz tube was first evacuated before heating until a pressure of 10^{-8} Torr, and no m/z signal above background was reached, with special scrutiny on water and air. For the data analysis, the QMS signal was normalized to the sample mass measured before heating the samples.

■ ASSOCIATED CONTENT

Supporting Information

The Supporting Information is available free of charge at https://pubs.acs.org/doi/10.1021/acsomega.1c04670.

PXRD pattern, FTIR spectra, TGA−DTA, TPD-mass spectrometer, and crystallographic data including refinement statistics, structural parameters, bond lengths, and angles of the iron compounds (PDF)

Compound **1** (CIF)

Compound **1** (CIF)

■ AUTHOR INFORMATION

Corresponding Authors

Godwin Severa − *Hawai'i Natural Energy Institute, University of Hawai'i at Mānoa, Honolulu, Hawaii 96822, United States*; orcid.org/0000-0002-1695-9123; Email: severa@hawaii.edu

Przemyslaw Dera − *Hawai'i Institute of Geophysics and Planetology, University of Hawai'i at Mānoa, Honolulu, Hawaii 96822, United States*; Email: pdera@hawaii.edu

Authors

Edward Bruffey − *Hawai'i Natural Energy Institute, University of Hawai'i at Mānoa, Honolulu, Hawaii 96822, United States*

Phuong Q. H. Nguyen − *Hawai'i Institute of Geophysics and Planetology, University of Hawai'i at Mānoa, Honolulu, Hawaii 96822, United States*

Angelina Gigante − *Département de Chimie Physique, Université de Genève, 1211 Geneva 4, Switzerland*; orcid.org/0000-0002-7226-1360

Noemi Leick − *National Renewable Energy Laboratory (NREL), Colorado, Colorado 80401, United States*; orcid.org/0000-0002-2014-6264

Colleen Kelly − *Hawai'i Natural Energy Institute, University of Hawai'i at Mānoa, Honolulu, Hawaii 96822, United States*

Gregory J. Finkelstein − *Hawai'i Institute of Geophysics and Planetology, University of Hawai'i at Mānoa, Honolulu, Hawaii 96822, United States*

Hans Hagemann − *Département de Chimie Physique, Université de Genève, 1211 Geneva 4, Switzerland*; orcid.org/0000-0002-7183-8543

Thomas Gennett − *National Renewable Energy Laboratory (NREL), Colorado, Colorado 80401, United States; Chemistry Department, Colorado School of Mines, Golden, Colorado 80401, United States*

Richard E. Rocheleau − *Hawai'i Natural Energy Institute, University of Hawai'i at Mānoa, Honolulu, Hawaii 96822, United States*

Complete contact information is available at: https://pubs.acs.org/10.1021/acsomega.1c04670

Notes

The authors declare no competing financial interest.

■ ACKNOWLEDGMENTS

The authors thank the Asia Pacific Research Initiative for Sustainable Energy Systems (APRISES) 2016 (Award No. N00014-17-1-2206) and 2014 (Award No. N00014-15-1-0028) and the University of Hawaii Materials Science Consortium for Research and Education (MSCoRE) for financial support. This research was supported, in part, by the Swiss National Science Foundation (project 200020-182494). The X-ray diffraction studies were performed using the X-ray Atlas instrument at the University of Hawaii, supported by NSF grant 1541516. The authors gratefully acknowledge research support from the Hydrogen Materials-Advanced Research Consortium (Hy-

MARC), established as part of the Energy Materials Network under the U.S. Department of Energy, Office of Energy Efficiency and Renewable Energy, Fuel Cell Technologies Office, under Contract DE-AC36-08GO28308.

REFERENCES

(1) Huang, Q.; Lee, Y.-Y.; Gurkan, B. Pyrrolidinium Ionic Liquid Electrolyte with Bis(trifluoromethylsulfonyl)imide and Bis-(fluorosulfonyl)imide Anions: Lithium Solvation and Mobility, and Performance in Lithium Metal−Lithium Iron Phosphate Batteries. *Ind. Eng. Chem. Res.* **2019**, *58*, 22587−22597.
(2) Greer, A. J.; Jacquemin, J.; Hardacre, C. Industrial Applications of Ionic Liquids. *Molecules* **2020**, *25*, No. 5207.
(3) Matsuoka, A.; Kamio, E.; Matsuyama, H. Investigation into the Effective Chemical Structure of Metal-Containing Ionic Liquids for Oxygen Absorption. *Ind. Eng. Chem. Res.* **2019**, *58*, 23304−23316.
(4) Maase, M. Industrial Applications of Ionic Liquids. In *Ionic Liquids in Synthesis*, 2nd ed.; Wasserscheid, P.; Welton, T., Eds.; Wiley-VCH Verlag GmbH & Co. KGaA, 2007; pp 663−687.
(5) Pucheault, M.; Vaultier, M. Task Specific Ionic Liquids and Task Specific Onium Salts. In *Topics in Current Chemistry*; Springer, 2009; Vol. *290*, pp 83−126.
(6) Lei, Z.; Dai, C.; Chen, B. Gas Solubility in Ionic Liquids. *Chem. Rev.* **2014**, *114*, 1289−1326.
(7) MacFarlane, D. R.; Tachikawa, N.; Forsyth, M.; Pringle, J. M.; Howlett, P. C.; Elliott, G. D.; Davis, J. H.; Watanabe, M.; Simon, P.; Angell, C. A. Energy applications of ionic liquids. *Energy Environ. Sci.* **2014**, *7*, 232−250.
(8) Smiglak, M.; Pringle, J. M.; Lu, X.; Han, L.; Zhang, S.; Gao, H.; MacFarlane, D. R.; Rogers, R. D. Ionic liquids for energy, materials, and medicine. *Chem. Commun.* **2014**, *50*, 9228−9250.
(9) Severa, G.; Head, J.; Bethune, K.; Higgins, S.; Fujise, A. Comparative studies of low concentration SO_2 and NO_2 sorption by activated carbon supported [C2mim][Ac] and KOH sorbents. *J. Environ. Chem. Eng.* **2018**, *6*, 718−727.
(10) Zazybin, A. G.; Rafikova, K.; Yu, V.; Zolotareva, D.; Dembitsky, V. M.; Sasaki, T. Metal-containing ionic liquids: current paradigm and applications. *Russ. Chem. Rev.* **2017**, *86*, 1254−1270.
(11) Lin, I. J. B.; Vasam, C. S. Metal-containing ionic liquids and ionic liquid crystals based on imidazolium moiety. *J. Organomet. Chem.* **2005**, *690*, 3498−3512.
(12) Chiappe, C.; Malvaldi, M. Highly concentrated "solutions" of metal cations in ionic liquids: current status and future challenges. *Phys. Chem. Chem. Phys.* **2010**, *12*, 11191−11196.
(13) Del Sesto, R. E.; McCleskey, T. M.; Burrell, A. K.; Baker, G. A.; Thompson, J. D.; Scott, B. L.; Wilkes, J. S.; Williams, P. Structure and magnetic behavior of transition metal based ionic liquids. *Chem. Commun.* **2008**, 447−449.
(14) Lui, M. Y.; Crowhurst, L.; Hallett, J. P.; Hunt, P. A.; Niedermeyer, H.; Welton, T. Salts dissolved in salts: ionic liquid mixtures. *Chem. Sci.* **2011**, *2*, 1491−1496.
(15) Wegner, S.; Janiak, C. Metal Nanoparticles in Ionic Liquids. In *Ionic Liquids II*; Topics in Current Chemistry Collections, 2018; Vol. *375*, pp 153−184.
(16) Dera, P.; Bruffey, E.; Finkelstein, G. J.; Kelly, C.; Gigante, A.; Hagemann, H.; Severa, G. Synthesis, Characterization, and Crystal Structures of Two New Manganese Aceto EMIM Ionic Compounds with Chains of Mn2+ Ions Coordinated Exclusively by Acetate. *ACS Omega* **2020**, *5*, 15592−15600.
(17) Rogers, R. D.; Seddon, K. R. Ionic Liquids–Solvents of the Future? *Science* **2003**, *302*, 792−793.
(18) Ghandi, K. A Review of Ionic Liquids, Their Limits and Applications. *Green Sustainable Chem.* **2014**, *4*, 44−53.
(19) Irge, D. D. Ionic Liquids: A Review on Greener Chemistry Applications, Quality Ionic Liquid Synthesis and Economical Viability in a Chemical Processes. *Am. J. Phys. Chem. A.* **2016**, *5*, 74−79.
(20) Meng, T.; Young, K.-H.; Wong, D. F.; Nei, J. Ionic Liquid-Based Non-Aqueous Electrolytes for Nickel/Metal Hydride Batteries. *Batteries* **2017**, *3*, No. 4.
(21) Matsumoto, K.; Hagiwara, R.; Mazej, Z.; Benkič, P.; Žemva, B. Crystal structures of frozen room temperature ionic liquids, 1-ethyl-3-methylimidazolium tetrafluoroborate ($EMImBF_4$), hexafluoroniobate ($EMImNbF_6$) and hexafluorotantalate ($EMImTaF_6$), determined by low-temperature X-ray diffraction. *Solid State Sci.* **2006**, *8*, 1250−1257.
(22) Dean, P. M.; Pringle, J. M.; MacFarlane, D. R. Structural analysis of low melting organic salts: perspectives on ionic liquids. *Phys. Chem. Chem. Phys.* **2010**, *12*, 9144−9153.
(23) Zhao, Y.; Hu, X.; Zhang, Q.; Guan, P. Crystal structure and aggregation behavior in water of ionic liquid 1-hexadecyl-3-methyl-imidazolium Bromide. *Mater. Lett.* **2010**, *64*, 794−797.
(24) Austen Angell, C.; Ansari, Y.; Zhao, Z. Ionic Liquids: Past, present and future. *Faraday Discuss.* **2012**, *154*, 9−27.
(25) Wang, C.; Cui, G.; Luo, X.; Xu, Y.; Li, H.; Dai, S. Highly Efficient and Reversible SO_2 Capture by Tunable Azole-Based Ionic Liquids through Multiple-Site Chemical Absorption. *J. Am. Chem. Soc.* **2011**, *133*, 11916−11919.
(26) James, S. L. The Dam Bursts for Porous Liquids. *Adv. Mater.* **2016**, *28*, 5712−5716.
(27) Hayes, R.; Warr, G. G.; Atkin, R. Structure and Nanostructure in Ionic Liquids. *Chem. Rev.* **2015**, *115*, 6357−6426.
(28) Anthony, J. L.; Anderson, J. L.; Maginn, E. J.; Brennecke, J. F. Anion Effects on Gas Solubility in Ionic Liquids. *J. Phys. Chem. B* **2005**, *109*, 6366−6374.
(29) Severa, G.; Bethune, K.; Rocheleau, R.; Higgins, S. SO_2 sorption by activated carbon supported ionic liquids under simulated atmospheric conditions. *Chem. Eng. J.* **2015**, *265*, 249−258.
(30) Froschauer, C.; Weber, H. K.; Röder, T.; Sixta, H.; Laus, G.; Lendl, B.; Schottenberger, H. No Matter of Course: Ionic Liquids as SO_2-Selective Gas Absorbers. *Lenzinger Ber.* **2013**, *91*, 30−43.
(31) Bowron, D. T.; D'Agostino, C.; Gladden, L. F.; Hardacre, C.; Holbrey, J. D.; Lagunas, M. C.; McGregor, J.; Mantle, M. D.; Mullan, C. L.; Youngs, T. G. A. Structure and Dynamics of 1-Ethyl-3-methylimidazolium Acetate via Molecular Dynamics and Neutron Diffraction. *J. Phys. Chem. B* **2010**, *114*, 7760−7768.
(32) Oliveira, F. S.; Cabrita, E. J.; Todorovic, S.; Bernardes, C. E. S.; Canongia Lopes, J. N.; Hodgson, J. L.; MacFarlane, D. R.; Rebelo, L. P. N.; Marrucho, I. M. Mixtures of the 1-ethyl-3-methylimidazolium acetate ionic liquid with different inorganic salts: insights into their interactions. *Phys. Chem. Chem. Phys.* **2016**, *18*, 2756−2766.
(33) Serov, N. Y.; Shtyrlin, V. G.; Islamov, D.; Kataeva, O. N.; Krivolapov, D. B. Structure of copper(II) complexes grown from ionic liquids − 1-ethyl-3-methylimidazolium acetate or chloride. *Acta Crystallogr., Sect. E: Crystallogr. Commun.* **2018**, *74*, 981−986.
(34) Nakamoto, K. Theory of Normal Vibrations. In *Infrared and Raman Spectra of Inorganic and Coordination Compounds*, 6th ed.; Nakamoto, K., Ed.; John Wiley & Sons, Inc., 2008; pp 1−147.
(35) Nakamoto, K. Applications in Inorganic Chemistry. In *Infrared and Raman Spectra of Inorganic and Coordination Compounds*, 6th ed.; Nakamoto, K., Ed.; John Wiley & Sons, Inc., 2008; pp 149−354.
(36) Alcock, N. W.; Tracy, V. M.; Waddington, T. C. Acetates and acetato-complexes. Part 2. Spectroscopic studies. *J. Chem. Soc., Dalton Trans* **1976**, 2243−2246.
(37) Deacon, G. B.; Phillips, R. J. Relationships between the carbon-oxygen stretching frequencies of carboxylato complexes and the type of carboxylate coordination. *Coord. Chem. Rev.* **1980**, *33*, 227−250.
(38) Ito, K.; Bernstein, H. J. The vibrational spectra of the formate, acetate, and oxalate ions. *Can. J. Chem* **1956**, *34*, 170−178.
(39) Oppenheimer, S. M.; Sushkov, A. B.; Musfeldt, J. L.; Achey, R. M.; Dalal, N. S. Diffuse optical excitations in Mn_{12}-acetate. *Phys. Rev. B* **2002**, *65*, No. 054419.
(40) Edwards, H. G. M.; Lewis, I. R. Vibrational spectroscopic studies of iron(II) acetate. *J. Mol. Struct.* **1993**, *296*, 15−20.
(41) Dhumal, N. R.; Kim, H. J.; Kiefer, J. Molecular Interactions in 1-Ethyl-3-methylimidazolium Acetate Ion Pair: A Density Functional Study. *J. Phys. Chem. A* **2009**, *113*, 10397−10404.

https://doi.org/10.1021/acsomega.1c04670
ACS Omega 2021, 6, 31907−31918

(42) Thomas, M.; Brehm, M.; Hollóczki, O.; Kelemen, Z.; Nyulászi, L.; Pasinszki, T.; Kirchner, B. Simulating the vibrational spectra of ionic liquid systems: 1-Ethyl-3-methylimidazolium acetate and its mixtures. *J. Chem. Phys.* **2014**, *141*, No. 024510.
(43) Clough, M. T.; Geyer, K.; Hunt, P. A.; Mertes, J.; Welton, T. Thermal decomposition of carboxylate ionic liquids: trends and mechanisms. *Phys. Chem. Chem. Phys.* **2013**, *15*, 20480−20495.
(44) Černý, R.; Ravnsbæk, D. B.; Severa, G.; Filinchuk, Y.; D' Anna, V.; Hagemann, H.; Haase, D.; Skibsted, J.; Jensen, C. M.; Jensen, T. R. Structure and Characterization of $KSc(BH_4)_4$. *J. Phys. Chem. C* **2010**, *114*, 19540−19549.
(45) Paskevicius, M.; Jepsen, L. H.; Schouwink, P.; Černý, R.; Ravnsbæk, D. B.; Filinchuk, Y.; Dornheim, M.; Besenbacher, F.; Jensen, T. R. Metal borohydrides and derivatives − synthesis, structure and properties. *Chem. Soc. Rev.* **2017**, *46*, 1565−1634.
(46) Cao, Y.; Mu, T. Comprehensive Investigation on the Thermal Stability of 66 Ionic Liquids by Thermogravimetric Analysis. *Ind. Eng. Chem. Res.* **2014**, *53*, 8651−8664.
(47) King, A. W. T.; Parviainen, A.; Karhunen, P.; Matikainen, J.; Hauru, L. K. J.; Sixta, H.; Kilpeläinen, I. Relative and inherent reactivities of imidazolium-based ionic liquids: the implications for lignocellulose processing applications. *RSC Adv.* **2012**, *2*, 8020−8026.
(48) Wendler, F.; Todi, L.-N.; Meister, F. Thermostability of imidazolium ionic liquids as direct solvents for cellulose. *Thermochim. Acta* **2012**, *528*, 76−84.
(49) Elmasry, M. A. A.; Gaber, A.; Khater, E. M. H. Thermal decomposition of Ni(II) and Fe(III) acetates and their mixture. *J. Therm. Anal.* **1996**, *47*, 757−763.
(50) Laurikėnas, A.; Barkauskas, J.; Reklaitis, J.; Niaura, G.; Baltsknas, D.; Kareiva, A. Formation peculiarities of iron (III) acetate: potential precursor for iron metal-organic frameworks (MOFs). *Lith. J. Phys.* **2016**, *56*, 35−41.
(51) Hurst, K. E.; Heben, M. J.; Blackburn, J. L.; Gennett, T.; Dillon, A. C.; Parilla, P. A. A dynamic calibration technique for temperature programmed desorption spectroscopy. *Rev. Sci. Instrum.* **2013**, *84*, No. 025103.

https://doi.org/10.1021/acsomega.1c04670
ACS Omega 2021, 6, 31907−31918